

Fast 3D multichannel deconvolution of electromagnetic induction loop-loop apparent conductivity data sets acquired at low induction numbers

Julien Guillemoteau¹, Niels Bøie Christensen², Bo Holm Jacobsen², and Jens Tronicke¹

ABSTRACT

Electromagnetic induction (EMI) sensors using sufficiently low-frequency harmonic sources and sufficiently small loop separations operate in the low-induction-number (LIN) domain for a relatively wide range of background conductivity. These systems are used in diverse near-surface investigations including applications from soil sciences, hydrology, and archaeology. The special case of portable multiconfiguration EMI sensors operating at frequencies ≤ 20 kHz offers the possibility of using a fast linear deconvolution method to interpret multichannel data sets in three dimensions. Here, we have developed a fast 3D inversion/deconvolution method regularized with 3D smoothness constraints and formulated in the hybrid spectral-spatial domain. Compared with

other linear approaches, the spectral-spatial domain formulation significantly reduces the computational cost of the processing and opens the door for real-time 3D interpretation of large data sets consisting of more than 100,000 data points. First, we test our proposed algorithm on synthetic data sets computed with the full Maxwell theory. Then, we apply our method to a real four-configuration EMI data set acquired to map the thickness of peat layers embedded in a sandy environment. For the synthetic and the field example, we compared our result with the result obtained using a standard point-by-point 1D nonlinear inversion approach. This comparison demonstrates that the proposed methodology provides superior lateral resolution compared with the 1D nonlinear inversion, at the same time significantly reducing the computational cost of the processing.

INTRODUCTION

Portable loop-loop electromagnetic induction (EMI) sensors operating with harmonic source waveforms (frequency-domain electromagnetics) are increasingly used to rapidly map the electrical properties of the uppermost meters of the subsurface for a wide range of applications. In precision agriculture, Jadoon et al. (2015) invert data measured by a three-offset loop-loop system used with the horizontal and vertical coplanar (HCP and VCP) loop configurations in an irrigated agricultural field site in Saudi Arabia. Rudolph et al. (2016) investigate how apparent conductivities measured by portable EMI sensors could be incorporated in the statistical analysis of an agricultural experiment. Pedrera-Parrilla et al. (2016) analyze the effect of the near-surface water saturation in delineating soil heterogeneities at an olive tree plantation in Spain. There is also a growing interest in soil hydrologic studies. In a recent review of soil hydrology

methodologies (Vereecken et al., 2015), it is suggested that portable EMI sensors have considerable potential for studying the variability of bedrock depth, which is critical for subsurface lateral water flow. In von Hebel et al. (2014), it is also suggested that EMI sensor time-lapse surveys have the potential for characterizing hydrologically active layers. Some recent studies also showcased a more direct link between hydrologic parameter and portable EMI sensor data. For example, Rezaei et al. (2016) study the link between EMI electrical conductivity and hydraulic conductivity in a sandy agricultural area in Belgium. Furthermore, portable EMI systems are considered for detecting and mapping buried metallic objects in civil engineering including searching for unexploded ordnances (Shubitidze et al., 2005; McKenna and McKenna, 2010). Recently, Guillemoteau and Tronicke (2015) studied the optimal system orientation of a single-offset portable EMI sensor to map buried utility pipes at the Horstwalde test site (Germany). El-Qady et al. (2014) evaluate the appli-

Manuscript received by the Editor 6 October 2016; revised manuscript received 30 June 2017; published ahead of production 24 August 2017; published online 19 October 2017.

¹University of Potsdam, Institute of Earth and Environmental Sciences, Potsdam-Golm, Germany. E-mail: julien@geo.uni-potsdam.de; jens@geo.uni-potsdam.de.

²University of Aarhus, Department of Geoscience, Aarhus, Denmark. E-mail: nbc@geo.au.dk; bo@geo.au.dk.

© 2017 Society of Exploration Geophysicists. All rights reserved.

cation of a multifrequency portable EMI sensor for mapping buried pipelines. For years, portable EMI sensors have also been used in the field of archaeological prospecting (Scollar et al., 1990). Recently, De Smedt et al. (2014) use multiconfiguration EMI data to study the prehistoric landscape at Stonehenge (England), Dabas et al. (2016) compare the result of multiconfiguration EMI data inversion with electrical resistivity tomography at the archeological site of Vieil Evreux (France), and Simon et al. (2015) investigate the effect of magnetic viscosity on multifrequency portable EMI sensor data acquired at two archeological sites on the Thessaly plain (Greece). In addition, the growing interest of portable EMI sensors is also documented by applications in littoral (Weymer et al., 2015) and cryosphere studies (Dafflon et al., 2016; Hunkeler et al., 2016).

Multiconfiguration portable EMI systems allow for simultaneous acquisition of data with different loop separations and thereby different volumes of penetration. The recent development of preprocessing tools improving data quality (Delefortrie et al., 2014, 2016; Thiesson et al., 2014) and improvements in positioning precision (Böniger and Tronicke, 2010; Guillemoteau and Tronicke, 2015) allow for interpreting the data sets with imaging routines, which jointly invert multichannel data sets. Up to now, most imaging approaches have assumed a horizontally layered medium (Saey et al., 2012; Grellier et al., 2013; von Hebel et al., 2014; Davies et al., 2015; Guillemoteau et al., 2016) because (1) the spatial sampling density is typically not sufficient for 2D/3D inversion approaches and (2) it is not practical to completely process and invert large data sets (more than 100,000 data points) with robust 2D or 3D approaches due to the great computational cost.

A typical EMI data set is composed of several hundred thousand data points distributed over several hectares (ha). Inverting such a data set in 3D with a grid resolution of 10–20 cm requires a parameter space consisting of more than several tens of million model parameters. Even with relatively fast approximate methods such as those presented by Pérez-Flores et al. (2001, 2012) or Kamm et al. (2013), such 3D inversion efforts would require large computational costs and memory usage. To overcome these limitations, Guillemoteau and Tronicke (2015, 2016) have developed and evaluated an approximate 3D forward-modeling algorithm based on the Born approximation starting from a homogeneous half-space, which is formulated in the hybrid spectral-spatial domain. This formulation allows forward modeling of more than 100,000 data points recorded across several 10,000 m² within a minute. For low induction numbers (LINs) and for nonmetallic bodies with sizes smaller than the skin depth, this approximate forward-modeling approach allows the characterization of the structural properties of the subsurface conductivity distribution (Guillemoteau and Tronicke, 2016).

For the special case of low frequencies ($f < 20$ kHz) and small loop offsets ($s \leq 2$ m), isolated nonmetallic bodies are typically much smaller than the skin depth, and the LIN condition is fulfilled in a relatively wide range of electrical conductivity backgrounds. Such scenarios represent typical subsurface settings as encountered in soil sciences, archaeological, and hydrologic applications. In this study, we propose to use the forward-modeling approach presented and evaluated by Guillemoteau and Tronicke (2016) to reduce the computational cost required for performing a 3D inversion of portable EMI data sets. We also formulate the inverse problem in the hybrid spectral-spatial domain and apply the multichannel deconvolution (MCD) method as presented for the 2D direct current (DC) problem by Møller et al. (2001).

In the following, we first recall the theory and the limitations of the used forward-modeling approach. Then, we present our formulation of the related inverse problem based on the MCD approach. After that, we apply our 3D MCD method to synthetic data sets simulated with the full Maxwell theory by the integral equation (IE) method. Finally, we apply our 3D MCD approach to a multiconfiguration EMI field data set acquired in Paulinenaue, Germany, and we compare the results with ground truth data collected in boreholes. Although the presented MCD inversion approach is an approximation, the only practical alternative is a 1D inversion with vertical and lateral constraints. Thus, for the synthetic and field data sets, the results of our MCD approach are compared with the results obtained using a full accuracy, point-by-point 1D nonlinear inversion method. After evaluating and discussing our results, we provide some final conclusions.

FORWARD MODELING

Motivation

Our approximate 3D forward modeling is based on the linearity between the subsurface electrical conductivity and the observed apparent LIN conductivity provided by a loop-loop EMI sensor. The validity of this assumption breaks down, i.e., the problem is nonlinear, for the following cases:

- when the amplitude of the electric field associated to the eddy current shows a noticeable dependence on the frequency and the conductivity within the volume investigated by the sensor
- when the electric field associated to the eddy current shows a significant change of polarization at interfaces within the volume investigated by the sensor.

The effect of subsurface conductivity and the frequency on the electric field amplitude can be evaluated for the conductive half-space background with the LIN criterion given by (J. D. McNeill, 1980, Geonics Ltd. Tech., note TN-6)

$$s\sqrt{\omega\mu\sigma/2} \ll 1, \quad (1)$$

where s is the loop separation, ω is the angular frequency, μ is the magnetic permeability, and σ is the subsurface electrical conductivity. Habashy et al. (1993) also provide a criterion to evaluate the same effect for the case of an isolated body

$$|k_{\text{bgd}}|^2 D^2 \delta \ll 1, \quad (2)$$

where $k_{\text{bgd}} = \sqrt{-i\mu\omega\sigma}$ is the wavenumber of the background when assuming a diffusive regime, D is the size of the anomalous body, and δ is the ratio of conductivity between the anomalous body and the background medium. For the special case of portable loop-loop EMI sensor using a rather low frequency (<20 kHz) and a rather small loop separation (≤ 2 m), these conditions are valid for a wide range of scenarios dealing with nonmetallic targets.

The second source of nonlinearity, which is associated with the change of electric field polarization at interfaces, is defined as the depolarization effect by West and Macnae (1991). Such an effect does not occur for the case of a horizontally layered medium as the electric field induced inside the subsurface is parallel to the interfaces. Guillemoteau and Tronicke (2016) confirm this feature by showing that their linear 3D forward-modeling method provides ac-

curate responses comparable with the responses of a nonlinear 1D forward-modeling approach for cases in which conditions 1 and 2 are fulfilled. For 2D/3D subsurface settings, this depolarization effect is present. For cases fulfilling conditions 1 and 2, Guillemoteau and Tronicke (2016) also find that linear 3D forward modeling (1) is capable of modeling the structure and bulk conductivity for 2D/3D resistive isolated bodies (with respect to the background setting) and (2) is capable of characterizing the structure of conductive isolated 2D/3D bodies (with respect to background setting) but it underestimates their true electrical conductivity. These results show that the depolarization effect is critical for conductive isolated bodies. However, in both scenarios, the approximate 3D forward-modeling approach allows for a correct structural characterization of the subsurface conductivity distribution.

Finally, when the conditions given in equations 1 and 2 are fulfilled, the approximate 3D forward-modeling method is as reliable as a nonlinear 1D forward-modeling method in a horizontally layered setting, and, for 2D/3D settings, it allows the correct characterization of the structural properties of the subsurface conductivity distribution. Encouraged by these findings, we now pursue the implementation of a 3D inversion algorithm based on the forward-modeling approach as presented in details by Guillemoteau and Tronicke (2016).

LIN loop-loop system response

The LIN apparent conductivity reading σ_a (J. D. McNeill, 1980, Geonics Ltd. Tech., note TN-6) of a portable EMI sensor can be modeled by (Guillemoteau and Tronicke, 2015, 2016)

$$\sigma_{a,i}(x', y') = C \iiint \psi^i(x' - x, y' - y, z) \sigma(x, y, z) dx dy dz, \tag{3}$$

where $\psi^i(x, y, z)$ represents the 3D Fréchet kernel of the acquisition configuration i , which describes the instrument height, the loop separation, the loop-loop geometry, and the orientation of the instrument, and $\sigma(x, y, z)$ is the subsurface conductivity distribution. The function C is a constant given by (Guillemoteau and Tronicke, 2016)

$$C = -\frac{16 \pi s}{\mu^2 \omega^2 m^2}, \tag{4}$$

where m is the magnetic moment of the source. In equation 3, (x', y') are the lateral coordinates of the measurement (e.g., the position of the midpoint between the two loops) at a fixed height above the earth surface. In Figure 1, we show a sketch illustrating the geometry and the scale of the considered 3D problem. In addition, in Figure 2, we show a sketch illustrating equation 3 for the case of a profile of a multiconfiguration EMI sensor above an isolated conductive structure. For a constant instrument configuration operating in the LIN domain, ψ^i can be considered as weakly dependent on the subsurface conductivity distribution and can be evaluated by using the reciprocity theorem introduced by McGillivray et al. (1994) for the case of a homogeneous half-space. Tølbøll and

Christensen (2007) use this method to evaluate the sensitivity of airborne loop-loop systems, and Guillemoteau et al. (2015b) use it for studying the sensitivity of ground-based, large-offset SLINGRAM systems. For the present case, the sensitivity function is given by

$$\psi^i(x, y, z) = \text{Re}\{\mathbf{E}_t^i \cdot \mathbf{E}_r^i\}, \tag{5}$$

where \mathbf{E}_t^i is the electric field induced into a low-conductivity half-space by a transmitter and \mathbf{E}_r^i is a pseudoelectric field generated by a magnetic dipole with the position and orientation of the receiver. The formulas for computing the electric field generated inside a homogeneous half-space are given by Tølbøll and Christensen (2007), Guillemoteau et al. (2015a), and Guillemoteau and Tronicke (2015), where they are derived from a Schelkunoff potential formulation (Ward and Hohmann, 1988). When the LIN condition is fulfilled, the skin depth of \mathbf{E}^i is much larger than the extent of the illuminated volume. Thus, small-scale variations (<0.5 s) of electrical conductivity have a negligible effect on the amplitude of \mathbf{E}^i , and the Born approximation is widely applicable. By following the criterion provided by Habashy et al. (1993) to evaluate the limits of the Born approximations (equation 2), this conductivity variation can be larger for smaller 3D anomalous bodies and lower operating frequencies. As stated above, the special case of a multiconfiguration EMI instrument using rather low frequencies (<20 kHz) and a rather small loop separation (≤ 2 m) is well-adapted to the proposed method. Indeed, the relation between the LIN conductivity data recorded by such instruments and the real conductivity distribution occurring inside the integral in equation 3 can be considered as quasilinear for a large range of typical scenarios encountered in soil science, hydrologic, and archaeological applications. However, its validity is limited for systems using rather high frequencies (>20 kHz), in conductive environments (>0.5 S/m), and for specific applications such as modeling the response of highly conductive (e.g., metallic) objects, i.e., in cases in which conditions 1 or 2 are not fulfilled.

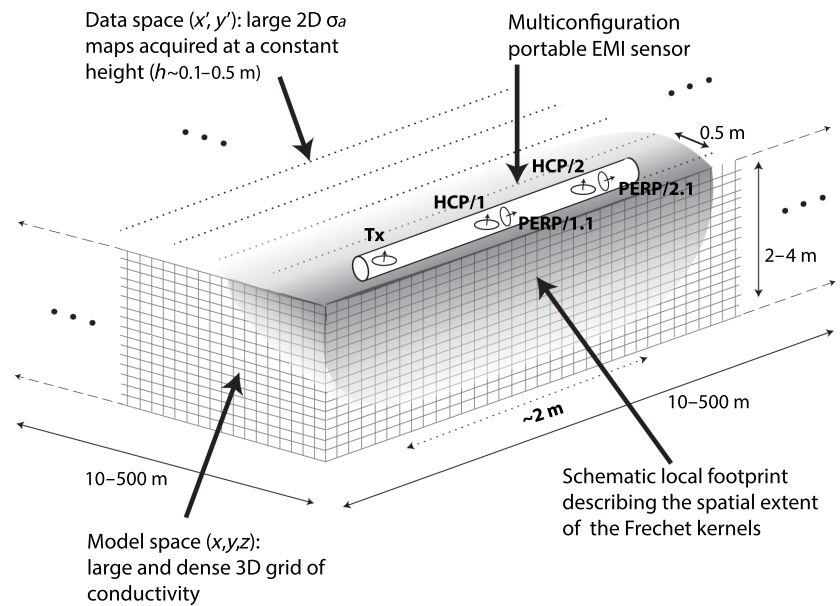


Figure 1. Sketch illustrating the 3D problem for interpreting apparent conductivity maps collected with a portable multiconfiguration EMI sensor. The volume illuminated by the system is much smaller than the total volume of the problem.

Forward model in the hybrid spectral-spatial (k_x, k_y, z) domain

The continuum expression in equation 3 is implemented in a discrete algorithm. We compute the LIN conductivity data provided by a LIN loop-loop sensor at a constant height h and at different lateral coordinates (x', y') above a 3D medium composed of $N_x \times N_y \times N_z$ rectangular cells. The 3D integral given in equation 3 also corresponds to a 1D integral over z of 2D convolution products in the xy -plane between infinitesimal layers of the Fréchet kernel and the corresponding layers of the 3D model of conductivity. To benefit from the properties of the convolution product in the spectral domain, we write this forward problem in the hybrid spectral-spatial domain (k_x, k_y, z) (where k_x and k_y are the spatial frequencies). First, the 3D distribution of conductivity $\sigma(x, y, z)$ is discretized into N_z layers. Within each layer l , the conductivity is assumed to be constant in the vertical direction, i.e., $\sigma_l(x, y, z) \rightarrow \sigma_l(x, y)$. Then, equation 3 can be written as (Guillemoteau and Tronicke, 2015, 2016)

$$\sigma_{a,i}(x', y') = C \sum_{l=1}^{N_z} \int \int_{-\infty}^{\infty} \psi_l^i(x' - x, y' - y) \sigma_l(x, y) dx dy. \quad (6)$$

Here, ψ_l^i is the 2D sensitivity function of the l th layer given by

$$\psi_l^i(x, y) = \int_{z^l}^{z^{l+1}} \psi^i(x, y, z) dz. \quad (7)$$

Equation 6 is a sum of double integrals. In the spectral domain (denoted with the \sim symbol), this simplifies to a sum of products:

$$\tilde{\sigma}_{a,i}(k_x, k_y) = C \sum_{l=1}^{N_z} \tilde{\psi}_l^i(k_x, k_y) \tilde{\sigma}_l(k_x, k_y), \quad (8)$$

where $\tilde{\psi}_l^i$ is the discrete Fourier transform of the $N_x \times N_y$ grid of sensitivity values in ψ_l^i . Then, the lateral distribution of the LIN apparent conductivity response in the space domain is obtained by performing the corresponding $N_x \times N_y$ discrete inverse Fourier transform of the resulting left hand side of equation 8.

INVERSE SOLUTION

The general objective of the inversion is to focus the measured LIN apparent conductivity data as sketched in Figure 2 into conductivity values centered correctly laterally and in depth.

Continuous space domain formulation

We consider the problem of jointly inverting N_c LIN apparent conductivity data maps, where N_c is the number of different configurations, i.e., different transmitter-receiver geometries such as HCP/VCP or perpendicular configurations with a receiver oriented in the inline direction (PERP), and variations in further acquisition parameters such as variations in loop separation s , system height h , or even the pitch, the roll, and the yaw (Guillemoteau and Tronicke, 2015) of the system. Figure 3a illustrates such conductivity maps for four different configurations ($N_c = 4$) characterized by the same system height, pitch, roll, and yaw, but by different loop geometries and loop separations (two PERP configurations with $s = 1.1$ m and $s = 2.1$ m and two HCP configurations with $s = 1$ m and $s = 2$ m noted by PERP/1.1, PERP/2.1, HCP/1, and HCP/2, respectively). Now, the tomographic problem is to retrieve the true distribution of conductivity $\sigma(x, y, z)$ inside the half-space having N_c observed data maps. Typically, such inverse problems suffer from instability due to data noise, systematic error, and the inherent smoothing in mapping the conductivity structure from a limited number of data points and configurations. This issue is usually handled by some combined minimization of data misfit and model constraints. For inverting DC data, Møller et al. (2001) invoke a Bayesian viewpoint following Tarantola and Valette (1982). In this study, we use a weighted sum of a data misfit L^2 -norm and standard smoothness constraints (Menke, 1989; Aster et al., 2005).

For each measurement position (x', y') , the data misfit term Φ_d measures the sum of the absolute differences between the observed multiconfiguration LIN apparent conductivities σ_a^{Obs} and the modeled conductivities σ_a^{Mod} :

$$|\Phi_d(x', y')|^2 = \sum_{i=1}^{N_c} [\sigma_{a,i}^{\text{Obs}}(x', y') - \sigma_{a,i}^{\text{Mod}}(x', y')]^2. \quad (9)$$

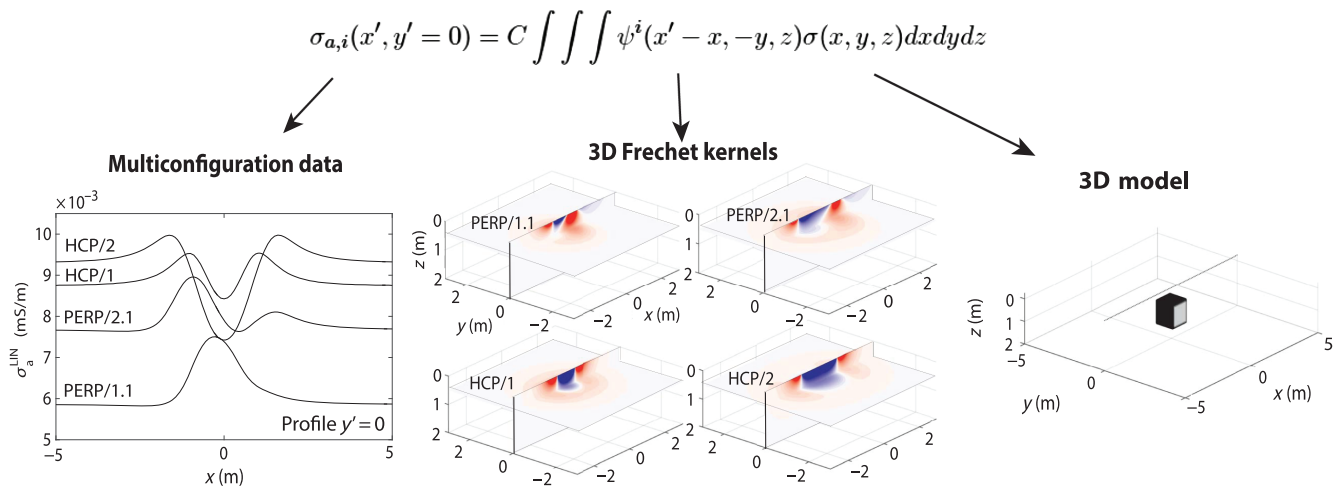


Figure 2. Sketch illustrating the linear 3D forward-modeling approach. Example for a profile of multiconfiguration data located at $y = 0$ m simulated above a cubic conductive formation.

The model parameter term Φ_m of the objective function is based on common smoothness constraints, and we define the first-order 1D difference function s_1 as

$$s_1(\nu) = \delta(\nu) - \delta(\nu + \Delta\nu), \quad (10)$$

where δ is the Dirac delta function and the variable ν can be either x , y , or z . Hence, at each lateral position of the model (x, y), the x -oriented spatial constraint term is the integral over z of the function $s_1(x)$ convolved with the 3D model conductivity:

$$|\Phi_m^x(x, y)|^2 = \lambda_x \int_0^\infty [s_1(x) * \sigma(x, y, z)]^2 dz. \quad (11)$$

Similarly, for the y - and z -directions, we have

$$|\Phi_m^y(x, y)|^2 = \lambda_y \int_0^\infty [s_1(y) * \sigma(x, y, z)]^2 dz \quad (12)$$

and

$$|\Phi_m^z(x, y)|^2 = \lambda_z \int_0^\infty [s_1(z) * \sigma(x, y, z)]^2 dz. \quad (13)$$

Here, λ_x, λ_y , and λ_z are the damping factors characterizing the relative importance of each model term with respect to the data misfit term. By assuming continuous measurements on a horizontal plane at a constant height h over the ground surface, the overall objective function Φ_g can be written as

$$\begin{aligned} \Phi_g = & \int_{-\infty}^\infty \int_{-\infty}^\infty |\Phi_d|^2 dx' dy' \\ & + \int_{-\infty}^\infty \int_{-\infty}^\infty (|\Phi_m^x|^2 + |\Phi_m^y|^2 + |\Phi_m^z|^2) dx dy. \end{aligned} \quad (14)$$

Continuous spectral-spatial (k_x, k_y, z) domain formulation

By defining the lateral coordinates of the model grid equal to the measurement grid, i.e., by defining $(x', y') = (x, y)$, and by using the Plancherel theorem (Rudin, 1987), the objective function of the tomographic problem given in equation 14 can be written as

$$\begin{aligned} \Phi_g = & \int_{-\infty}^\infty \int_{-\infty}^\infty |\tilde{\Phi}_d|^2 dk_x dk_y \\ & + \int_{-\infty}^\infty \int_{-\infty}^\infty (|\tilde{\Phi}_m^x|^2 + |\tilde{\Phi}_m^y|^2 + |\tilde{\Phi}_m^z|^2) dk_x dk_y. \end{aligned} \quad (15)$$

Here, and similarly for the forward model, the symbol $\tilde{\cdot}$ denotes the double spatial Fourier transform $\{x \rightarrow k_x, y \rightarrow k_y\}$. For each spectral position (k_x, k_y) , the data misfit term is

$$|\tilde{\Phi}_d(k_x, k_y)|^2 = \sum_{i=1}^{N_c} [\tilde{\sigma}_{a,i}^{Obs}(k_x, k_y) - \tilde{\sigma}_{a,i}^{Mod}(k_x, k_y)]^2, \quad (16)$$

and the model regularizing terms given in equations 11–13 become

$$|\tilde{\Phi}_m^x(k_x, k_y)|^2 = \lambda_x \int_0^\infty [\tilde{s}_1(k_x) \tilde{\sigma}(k_x, k_y, z)]^2 dz, \quad (17)$$

$$|\tilde{\Phi}_m^y(k_x, k_y)|^2 = \lambda_y \int_0^\infty [\tilde{s}_1(k_y) \tilde{\sigma}(k_x, k_y, z)]^2 dz, \quad (18)$$

and

$$|\tilde{\Phi}_m^z(k_x, k_y)|^2 = \lambda_z \int_0^\infty [\tilde{\sigma}(k_x, k_y, z) - \tilde{\sigma}(k_x, k_y, z + \Delta z)]^2 dz. \quad (19)$$

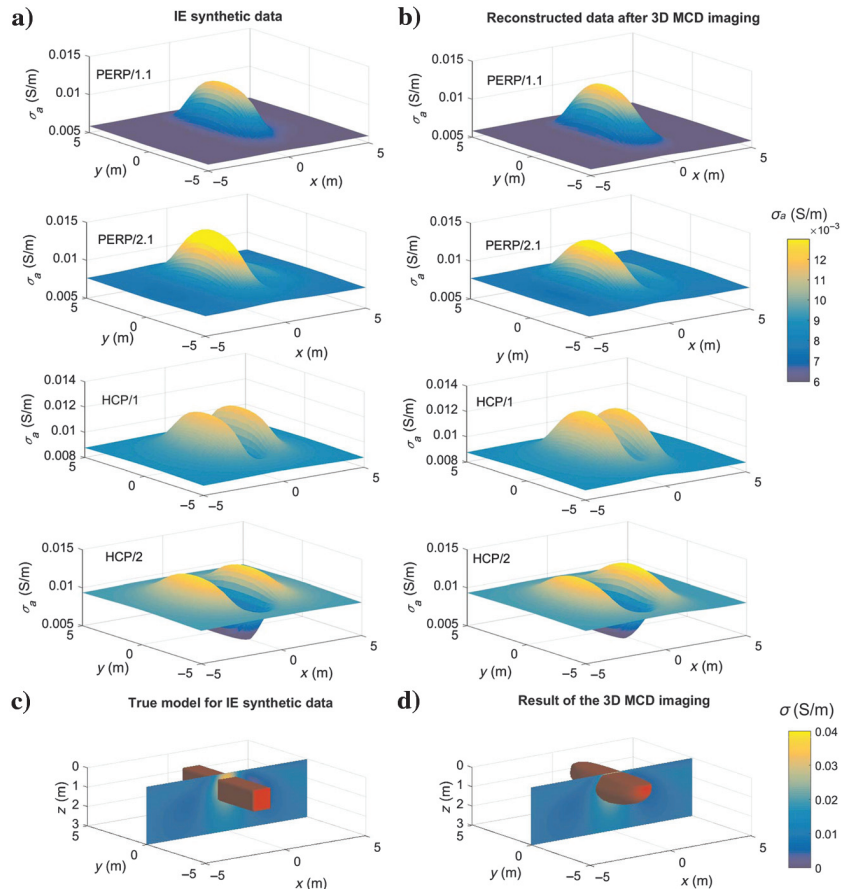


Figure 3. Inversion results of the 3D MCD method for a synthetic data set computed with the IE method. The input model is a rectangular block with a conductivity of $\sigma = 0.1$ S/m embedded in a homogeneous background with $\sigma = 0.01$ S/m. The block has a length of 5 m, a vertical cross section of 1×1 m, and it is centered at a depth of 0.8 m: (a) synthetic IE data, (b) modeled data after 3D MCD imaging, (c) geometry and position of the conductive rectangular block shown with the result of the 3D MCD imaging for a vertical slice at $y = 0$ m, and (d) result of the 3D MCD imaging. In (c and d), the red surface represents an isosurface for $\sigma = 0.025$ S/m.

The discrete spectral-spatial domain formulation

Data are acquired on a plane (x, y) with a constant configuration. In real data sets, the data space depends on the lateral sampling density. We consider a map of $N_x \times N_y$ multiconfiguration measurements acquired with lateral sampling intervals of Δx and Δy on a horizontal plane above a 3D conductive subsurface. The model space is discretized into small elements for which the conductivity is assumed to be constant. When the problem is posed in the (k_x, k_y, z) domain, it is necessary to use the same lateral discretization for the data and the model space. Therefore, the 3D model of conductivity is designed with rectangular cells of size Δx , Δy , and Δz over a 3D medium of volume $L_x \times L_y \times L_z$, where L_i is the size of the volume in direction i . It follows that the function $\tilde{\Phi}$ is sampled with a minimum interval of $\Delta k_x = 2\pi/L_x$ and $\Delta k_y = 2\pi/L_y$ in the spectral domain. Thus, once the model and data space are properly discretized, the data misfit term is given by

$$|\tilde{\Phi}_d(k_x, k_y)|^2 = \sum_{i=1}^{N_c} \left[\tilde{\sigma}_{a,i}^{\text{Obs}}(k_x, k_y) - C \sum_{l=1}^{N_z} \tilde{\psi}_i(k_x, k_y) \tilde{\sigma}_l(k_x, k_y) \right]^2. \quad (20)$$

For a finite number of layers, equations 17–19 are given by

$$|\tilde{\Phi}_m^x(k_x, k_y)|^2 = \lambda_x \sum_{l=1}^{N_z} D_l [\tilde{s}_1(k_x) \tilde{\sigma}_l(k_x, k_y)]^2, \quad (21)$$

$$|\tilde{\Phi}_m^y(k_x, k_y)|^2 = \lambda_y \sum_{l=1}^{N_z} D_l [\tilde{s}_1(k_y) \tilde{\sigma}_l(k_x, k_y)]^2, \quad (22)$$

and

$$|\tilde{\Phi}_m^z(k_x, k_y)|^2 = \lambda_z \left(\sum_{l=1}^{N_z-1} D_l [\tilde{\sigma}_l(k_x, k_y) - \tilde{\sigma}_{l+1}(k_x, k_y)]^2 + D_{N_z} [\tilde{\sigma}_{N_z-1}(k_x, k_y) - \tilde{\sigma}_{N_z}(k_x, k_y)]^2 \right), \quad (23)$$

where D_l corresponds to the thicknesses resulting from the vertical discretization. Hence, the damped least-squares problem minimizing $\tilde{\Phi} = |\tilde{\Phi}_d|^2 + |\tilde{\Phi}_m^x|^2 + |\tilde{\Phi}_m^y|^2 + |\tilde{\Phi}_m^z|^2$ for each spectral number (k_x, k_y) is equivalent to an ordinary least-squares problem (Aster et al., 2005) and can be written as

$$\min(\tilde{\Phi}(k_x, k_y)) = \min \left\| \begin{bmatrix} \tilde{\mathbf{G}}(k_x, k_y) \\ \mathbf{W}_m \end{bmatrix} \tilde{\sigma} - \begin{bmatrix} \tilde{\sigma}_a^{\text{Obs}}(k_x, k_y) \\ \mathbf{0} \end{bmatrix} \right\|^2. \quad (24)$$

Here, $\tilde{\mathbf{G}}(k_x, k_y)$ is a $N_c \times N_z$ matrix containing the function $\tilde{\psi}_i(k_x, k_y)$ and \mathbf{W}_m is a matrix of size $3N_z \times N_z$ containing the smoothness constraints, and it is given by

$$\mathbf{W}_m = \begin{bmatrix} \lambda_x \tilde{s}_1(k_x) \mathbf{D} \\ \lambda_y \tilde{s}_1(k_y) \mathbf{D} \\ \lambda_z \mathbf{DL} \end{bmatrix}, \quad (25)$$

where \mathbf{D} is a diagonal matrix containing thicknesses of the layers D_l and \mathbf{L} is the first-order 1D smoothness matrix applied to the vertical direction of the model. The solution $\tilde{\sigma}$ of the linear least-squares problem formulated in equation 24 is given as

$$\tilde{\sigma}(k_x, k_y) = (\tilde{\mathbf{G}}^T \tilde{\mathbf{G}} + \mathbf{S})^{-1} \tilde{\mathbf{G}}^T \tilde{\sigma}_a^{\text{Obs}}, \quad (26)$$

where the $N_z \times N_z$ smoothness matrix \mathbf{S} can be written as

$$\mathbf{S} = \mathbf{W}_m^T \mathbf{W}_m = \lambda_x^2 |\tilde{s}_1(k_x)|^2 \mathbf{D}^T \mathbf{D} + \lambda_y^2 |\tilde{s}_1(k_y)|^2 \mathbf{D}^T \mathbf{D} + \lambda_z^2 \mathbf{D}^T \mathbf{DL}. \quad (27)$$

By setting λ_x , λ_y , and λ_z to vary with the wavenumbers (k_x, k_y) , it is possible to impose a structural anisotropy at a selected scale. However, in our study, we simulate contexts with minimum a priori information. Therefore, we use a constant weight $\lambda = \lambda_x = \lambda_y = \lambda_z$ for all the wavenumbers. This means that we do not force the model to show some structural anisotropy at any scales of variation. The value of λ is selected using an OCCAM procedure (Constable et al., 1987); i.e., we take the largest value that fits the data according to a predefined amount of noise in the data set. As an example, for a final global root-mean-square (rms) error of 4%–5%, we found a value of $\lambda \approx 2 \pm 1$ for various synthetic data sets, and several real data sets collected at different field sites. After this problem is solved for each wavenumber (k_x, k_y) , the 3D distribution of the conductivity in the space domain is obtained by performing a double inverse Fourier transform of the solutions:

$$\sigma(x, y, [z_1 \cdots z_l \cdots z_{N_z}]) = \mathcal{F}^{-1}[\tilde{\sigma}(k_x, k_y)]. \quad (28)$$

Thus, we can see that when the problem is formulated in the (k_x, k_y, z) domain, the 3D inversion consists of performing $N_x \times N_y$ inversions with kernels of size $N_c \times N_z$. This method requires much less memory and is much faster than a 3D inversion in the space domain, which considers $N_c \times N_x \times N_y$ data and $N_x \times N_y \times N_z$ parameters that would require inversion of a $(N_c \times N_x \times N_y) \times (N_x \times N_y \times N_z)$ matrix.

SYNTHETIC EXAMPLES

We apply our MCD approach to a synthetic data set (Figure 3) computed using the program Marco440 (Raiche, 2008). Marco440 is based on a 3D IE method and can model EMI responses according to the full-accuracy Maxwell theory. In the example, we specifically look at the instrument used later on for collecting our field data (DUALEM21s), which measures four configurations simultaneously at a frequency of 9 kHz: two PERP (with a x -oriented receiver) configurations (PERP/1.1 and PERP/2.1) with loop separations of $s = 1.1$ m and $s = 2.1$ m, and two HCP configurations (HCP/1 and HCP/2) with $s = 1$ m and $s = 2$ m. The conductivity model (see Figure 3c) consists of a conductive rectangular block ($\sigma_p = 0.1$ S/m) elongated in the y -direction and embedded in a homogeneous background with a conductivity of $\sigma_b = 0.01$ S/m. The synthetic data set consists of four 40×40 m maps of x -directed lines with an inline sampling interval of $\Delta x = 0.1$ m and a crossline sampling interval of $\Delta y = 0.5$ m. In Figure 3a, we show the synthetic IE data for the four configurations acquired at a height of $h = 0.25$ m. The data maps are displayed for an area of 10×10 m centered across the conductive body. Following Guillemoteau and

Tronicke (2016), the used 3D forward-modeling approach needs a sufficiently dense data sampling and a minimum map size to avoid any artifacts resulting from the transformation to the spectral domain. Hence, for the inversion, the space and the data have been gridded with $0.1 \text{ m} \times 0.1 \text{ m} \times D_z$ blocks, where D_z corresponds to the thicknesses of 40 layers. The function D_z increases with depth to resemble the decrease in resolution with increasing depths of such surface-based EMI data. The size of the maps and the models is extended to $100 \times 100 \text{ m}$; i.e., data have been extrapolated. We set the extrapolated data equal to the background responses of each channel. The sensitivity functions for the 3D MCD were preliminarily computed for a frequency of 9 kHz, a height of $h = 0.25 \text{ m}$, and for a homogeneous half-space with a conductivity of $\sigma = 0.01 \text{ S/m}$. This setting corresponds to a rather LIN (≈ 0.03), and we can thus use the half-space sensitivity function for the LIN approximation.

The 3D MCD takes three minutes with a MATLAB code running on a single standard working station. The result of the MCD is a 3D model of electrical conductivity over the extended $100 \times 100 \text{ m}$ area, but it is shown in Figure 3d over a smaller area focusing on the anomalous body. We see that the isosurface $\sigma = 0.025 \text{ S/m}$ can retrieve the structure of the conductive body. A vertical slice of the solution located at $y = 0 \text{ m}$ is shown in Figure 3c and 3d with the true model that serves to compute the synthetic data. This synthetic example shows that the 3D MCD method permits a reconstruction of a realistic distribution of electrical conductivity in the ground from multiconfiguration signals recorded at the ground surface. However, the maximum value of conductivity shown in the final 3D image is approximately 0.04 S/m , which is less than the true electrical conductivity of the rectangular block. This result must be expected from the limitation of the forward-modeling approach (Guillemoteau and Tronicke, 2016).

We performed an additional test with a synthetic data set computed for the same four-configuration system, but for a more complex distribution of electrical conductivity and also using a realistic level of noise. The input model is a checkerboard-like structure embedded inside a layered medium (Figure 4). The background layered medium consists of two layers: a rather conductive surface layer ($\sigma_1 = 0.05 \text{ S/m}$) with thickness of $d_1 = 0.2 \text{ m}$ and a half-space with conductivity of $\sigma_2 = 0.01 \text{ S/m}$. The checkerboard structure is located in the second layer, and it is composed of $1 \times 1 \times 1 \text{ m}$ cubes with conductivity of $\sigma_c = 0.1 \text{ S/m}$. Similar to the previous synthetic example, data have been simulated by the IE method for a system height of $h = 0.25 \text{ m}$. The inline sampling is $\Delta x = 0.2 \text{ m}$, and the interline distance is $\Delta y = 0.5 \text{ m}$. The profiles are parallel to the x -direction, and the acquisition direction is toward increasing the x -coordinates. Gaussian noise with a standard deviation of 0.2 mS/m was added to the modeled data to simulate realistic field data. The modeled noisy data are shown in Figure 5a after interpolation to a $0.1 \times 0.1 \text{ m}$ grid.

We invert this data set by using our 3D MCD approach, and we compare the result with the result obtained by a point-by-point 1D nonlinear inversion approach. The 1D inversion was per-

formed using an in-house algorithm (Guillemoteau et al., 2016) with 25 layers and vertical smoothness constraints. For the 3D MCD method, we used the same sensitivity function characteristics as for the previous synthetic case (a frequency of 9 kHz, a system height of $h = 0.25 \text{ m}$, and $\sigma = 0.01 \text{ S/m}$). For the 3D and the 1D inversions, the synthetic data were fitted to within an rms error of 4%. The resulting modeled data are shown in Figure 5b and 5c. First, the 3D MCD approach is computationally more efficient than the 1D inversion of the full data set (minutes versus days). More importantly, comparison of the vertical (Figure 6a and 6b) and the horizontal slices (Figure 6c and 6d) demonstrates the benefit of the 3D MCD approach for imaging such a complex distribution of electrical conductivity. As expected, the 1D approach shows significant artifacts, whereas the smooth model provided by the 3D MCD approach focuses the local structure correctly in the horizontal directions. In the vertical slice, we see that neither of the 1D nor the 3D inversion approaches are able to accurately reconstruct the vertical variations present in the input model (e.g., the interface between the uppermost layer and the cubes) because our data sets are limited and, thus, do not allow us to resolve such details. On the other hand, such dual-configuration-type data sets (2 HCP and 2 PERP configurations) are less ambiguous for mapping small-scale lateral variations as demonstrated in Figure 6c, in which we notice that the final image is in good agreement with the true horizontal distribution of conductivity. Similar to the first synthetic example, the electrical conductivity of the cubes is underestimated relative to the true conductivity of the target due to the limited accuracy of the used forward-modeling approach and because of the constraints of the inversion. However, the conductivity of the uppermost layer is correctly estimated confirming that the present modeling approach is as precise as a standard nonlinear 1D method in a horizontally layered LIN context.

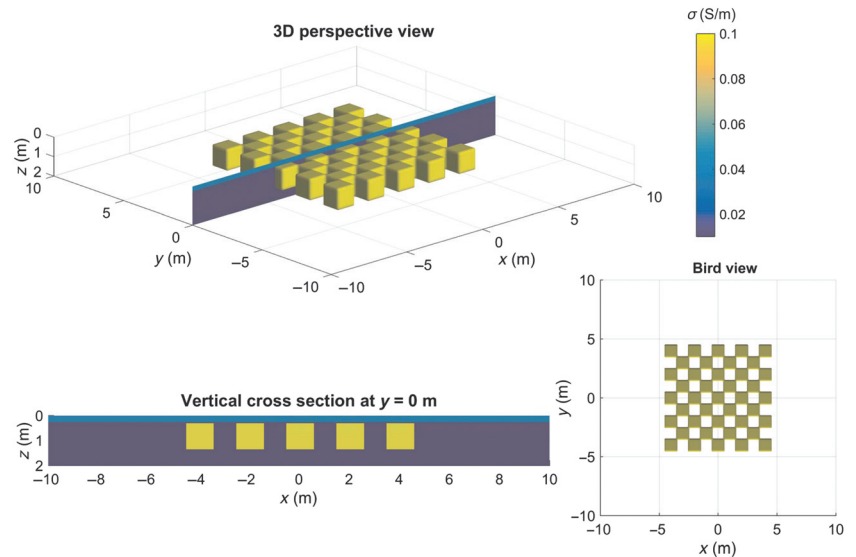


Figure 4. Different visualizations of the input model for the second synthetic example, composed of 41 conductive $1 \times 1 \times 1 \text{ m}$ cubes forming a checkerboard-like structure embedded inside a layered medium consisting of two homogeneous layers. The top of the cubes are located at a depth of $z = 0.3 \text{ m}$. The cubes are characterized by a conductivity of $\sigma_c = 0.1 \text{ S/m}$, and they are embedded in the second layer with a conductivity of $\sigma_2 = 0.01 \text{ S/m}$. The first layer of the background medium is characterized by a thickness of $d_1 = 0.2 \text{ m}$ and a conductivity of $\sigma_1 = 0.05 \text{ S/m}$.

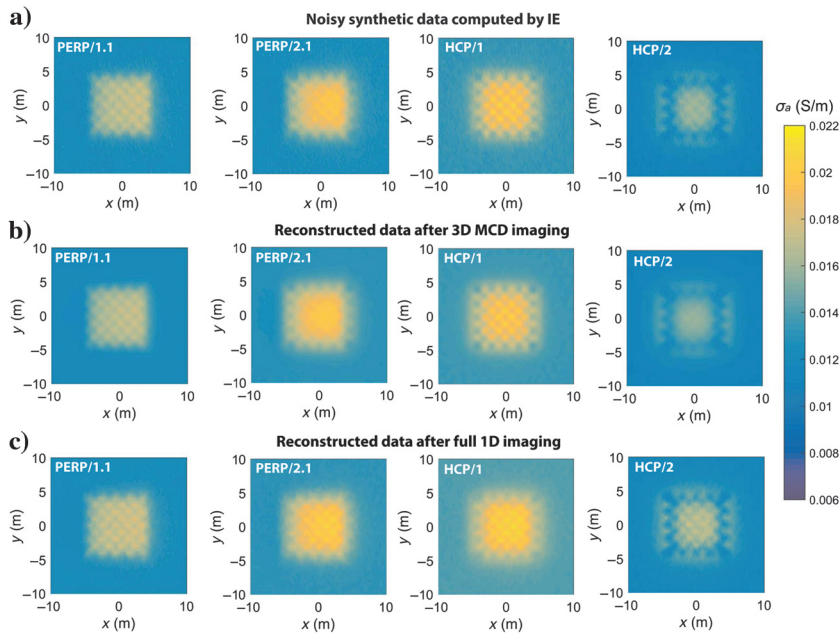


Figure 5. Comparison between (a) the input noisy synthetic data and the modeled data after (b) the fast 3D MCD method, and (c) the 1D nonlinear inversion. The 1D and 3D methods provide models that fit the synthetic data with an rms error of 4%.

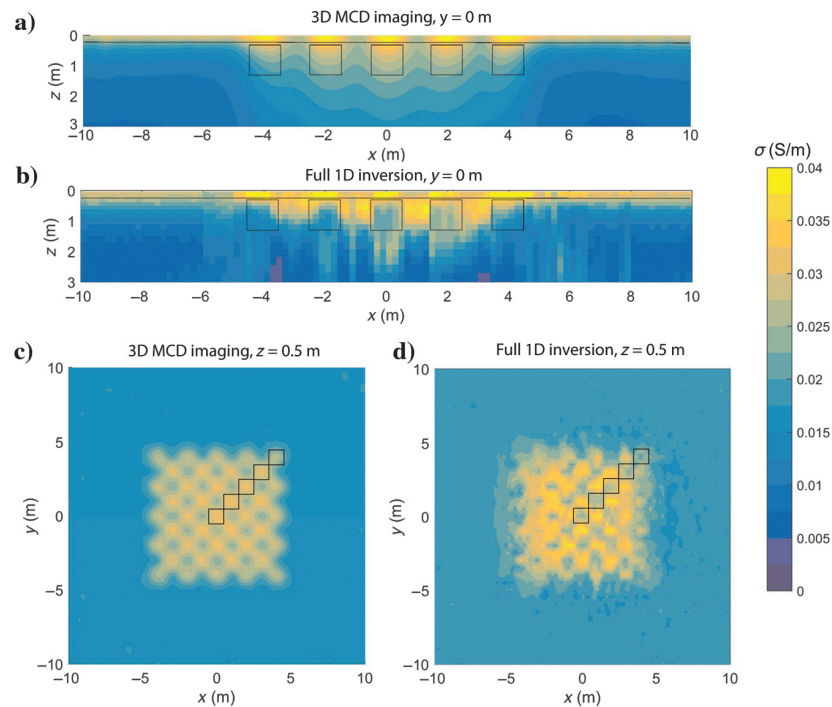


Figure 6. Comparison between (a) the fast 3D MCD imaging and (b) the point-by-point 1D nonlinear inversion for a vertical slice located at $y = 0$ m. Comparison between (c) the fast 3D inversion and (d) the point-by-point 1D nonlinear inversion for a horizontal slice located at $z = 0.5$ m. In panels (a and b), the true interface between the two layers and the surface of the cubes are shown by the black lines. In panels (c and d), the true lateral positions of five selected cubes are highlighted. Note that the 1D inversion produces a worst-case lateral resolution by modeling the conductive blocks exactly between the actual positions of the conductive blocks.

FIELD EXAMPLE

Now, we apply our 3D MCD approach to a field data set acquired in Paulinenaue, Germany, using a DUALEM21s instrument. As discussed in the previous section, the DUALEM21s operates at a frequency of 9 kHz with a maximum loop separation of 2.1 m. According to these parameters, our MCD approach is limited to environments with conductivities lower than <0.5 S/m because the induction number reaches a value of 0.28 for the $s = 2.1$ m channel. However, as discussed by Guillemoteau and Tronicke (2016), our forward-modeling approach can be applied in many archaeological or agricultural studies in which the electrical conductivity is often less than 0.5 S/m. This is the case for the field site studied here, which consists of peat layers and lenses deposited in a sandy background. In this area, the subsurface shows strong vertical and lateral changes of electrical conductivity between the sand (which can be rather dry near the surface) and the peat layers. However, the maximum measured apparent conductivity is approximately 0.1 S/m.

Acquisition and preliminary processing

In the field test of the MCD method, data were recorded at a constant height and with a regular lateral sampling as far as possible. The instrument was mounted on a cart to control and fix the instrument height as well as to reduce acquisition-related noise. During data acquisition, the position of the cart is measured by using a self-tracking total station comparable to Böniger and Tronicke (2010). Data are recorded at a rate of 5 Hz resulting in an inline data-point spacing of approximately 0.1 m. The distance between profiles is 0.5 m. This sampling density is sufficient to avoid artifacts, when interpolating the data onto a regular grid as required for applying our MCD approach. In the following, the x -axis is defined parallel to the profiles.

The recorded data set consists of $4 \times 97,470 = 389,880$ data points recorded across a nonsquare area, and it is shown in Figure 7a–7d after being interpolated onto a regular 0.1×0.1 m grid. The shape and the rather small size of the survey area illustrate the typical issues that have to be considered before applying the MCD method. First, our data have to be extrapolated over a larger square map to be accurately handled by our 3D MCD algorithm. We extrapolate the data to reduce the edge effect at the border of the actual area and to obtain a sufficient map size for the MCD approach. Note that because the footprint of the EMI system is small compared with the area covered by the maps, the extrapolated data have no influence on the result in which data have been recorded, except close to the border of the maps. In

addition, we have to consider that data were recorded in the vicinity of a metallic fence, and some manmade metallic objects are present in the subsurface (see Figure 7a–7d). Because the MCD approach is not adapted for imaging such small metallic objects and to limit the imaging artifacts related by these objects, the affected data are muted locally. Then, the resulting data gaps are reinterpolated. We also removed 4 m at the end of each profile to avoid artifacts related to the fence. The resulting data maps are shown in Figure 7e–7h. The range of measured LIN apparent conductivity values varies from 1–5 mS/m (in sand-dominated areas) to 50–100 mS/m (in peat-dominated areas).

In addition to the EMI measurements, 62 drillholes were available along nine profiles that are shown by the dashed lines in Figure 7a, and for one of the profiles ($y = 10$ m), a ground-penetrating radar (GPR) profile was collected. The drillholes were positioned across the peat deposit to evaluate its thickness. The GPR section was collected in the constant offset mode with a nominal center frequency of 100 MHz and processed using a basic standard processing flow including frequency filtering and amplitude scaling. Here, the GPR data serve to continuously detect the bottom of the peat layer between the drillholes along the profile $y = 10$ m. In addition to the GPR constant offset profile, several GPR common-midpoint (CMP) soundings were performed over the peat deposit to evaluate its GPR velocity.

Inversion results

The 3D inversion of the collected data set determines the electrical conductivity within a $100 \times 100 \times 50$ m grid with a sampling of $0.1 \text{ m} \times 0.1 \text{ m} \times D_z$, where D_z is the thickness of 40 layers that increases with depth. Thus, the parameter space consists of $1000 \times 1000 \times 40 = 40 \times 10^6$ cells. The 3D inversion of the $4 \times 1000 \times$

1000 interpolated data (originally 389,880 collected data points) for determining the electrical conductivity for these 40×10^6 parameters takes three minutes on a standard modern laptop computer. As a comparison, a point-by-point 1D nonlinear inversion of the original 389,880 data points with 40 layers takes some days in our MATLAB implementation. Optimized implementation will reduce this time, but still the 1D nonlinear inversion will take a significantly longer time. In Figure 8, we compare the result of the 3D inversion along the nine selected profiles with the peat-thickness data as provided by the drillholes. We see that the 3D MCD model is in accordance with the ground truth provided by the boreholes. Overall, the 3D inversion of this four-configurations EMI data set provides a good idea of the spatial extent of the dry sand ($\sigma < 0.01$ S/m), the saturated sand ($0.01 < \sigma < 0.03$ S/m), and the peat layers ($\sigma > 0.05$ S/m).

For a selected profile at $y = 10$ m, we also compare the result of the 3D inversion with the result of the 1D nonlinear inversions and a GPR profile acquired along the same line (Figure 9). In Figure 9a, the modeled data for the 1D and fast 3D EMI forward-modeling methods are compared with the observed data. The 1D and 3D inversion methods have been set to provide a comparable data fit with an rms within 4%–5%. In Figure 9b and 9c, respectively, we show the results of the point-by-point 1D stitched inversions along the profile and the result of the linear 3D inversion. In Figure 9d, we show the constant offset GPR profile. A time-to-depth conversion and a topographic correction have been performed assuming a constant GPR velocity of 0.04 m/ns, which has been derived from the analysis of the CMP soundings performed over the peat layer. A rather clear GPR reflector is related to the interface between the bottom of peat deposit and the sandy background. After the time-to-depth conversion, this reflector is in good agreement with the peat thickness data obtained by the drillholes along the considered profile. This result confirms the rather low GPR velocity in the peat layer.

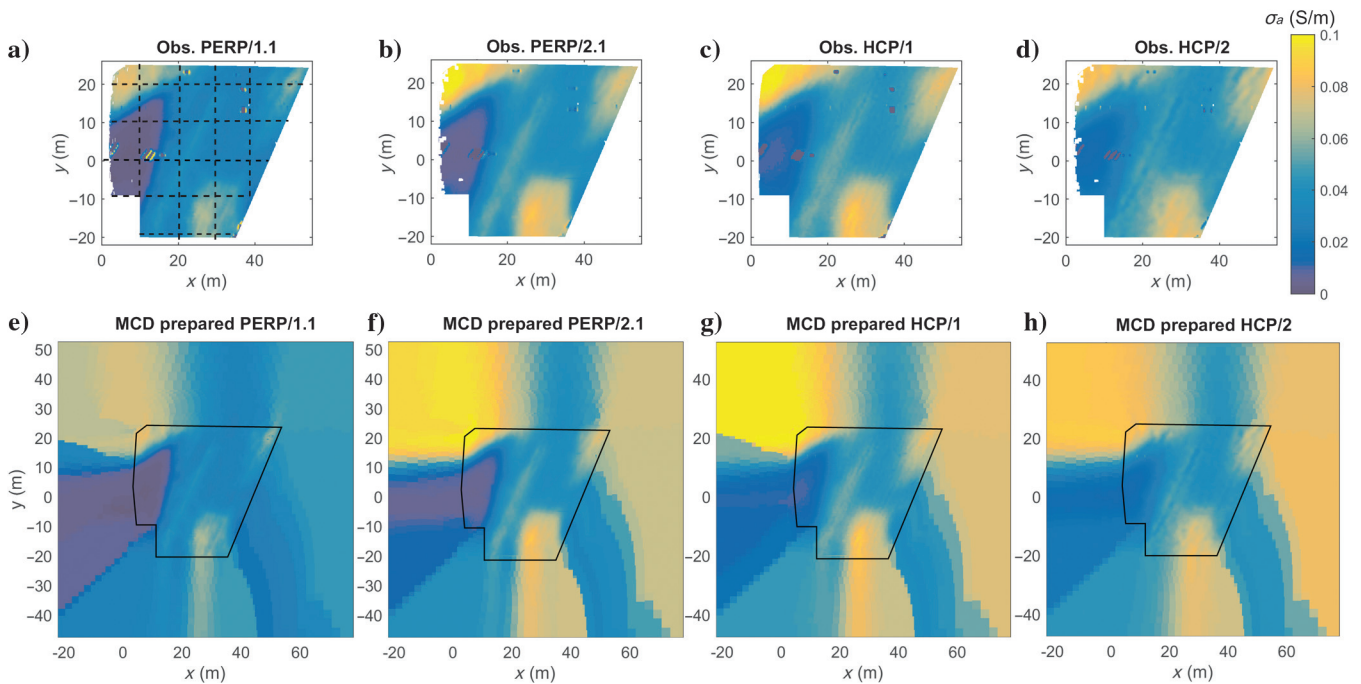


Figure 7. DUALEM21s data set collected in Paulinenaue, Brandenburg, Germany: (a–d) original data set contaminated by local anomalies related to metallic objects and (e–h) edited and extrapolated data in which isolated anomalies related to metallic objects have been removed. In panel (a), the dashed lines indicate the nine profiles in which the 62 drillhole soundings have been performed.

The depth to the bottom of the peat layer from the GPR profile is shown together with the drillholes results over the conductivity sections obtained by the inversion of EMI data in Figure 9b and 9c.

Overall, we see that the results of the 3D MCD method show better agreement with the drillholes and the GPR results than the results of the point-by-point 1D nonlinear inversion (compare Figure 9b and 9c). Indeed, despite a point-by-point data fit comparable with the data fit of the 3D MCD method, the 1D method shows several kinds of artifacts, which are not visible in the results of the 3D MCD method. The first kind corresponds to the rather slight lateral instability of the 1D inversion results (see the white circle in Figure 9b) inherent to a point-by-point inversion. Because these high-frequency lateral artifacts are weak and of limited scale, they are not critical for the geologic interpretation. It is possible to stabilize these small-scale lateral variations by using a laterally constrained 1D inversion approach (Santos, 2004; Auken et al., 2005). The second kind of artifact is more critical for the interpretation, and it is related to 2D/3D formations (see the rectangles highlighting several zones in Figure 9a and 9b). Zone 1 corresponds to a situation in which the system is over the resistive dry sand but starts to be sensitive to the nearby peat layers. For a given geometry, the larger the lateral extent of the illuminated volume, the earlier the peat layer is detected in the profile. Hence, we see (e.g., black dots in Figure 9a) that the HCP2 configuration is the first one to detect the peat layer along the profile, and that the PERP1.1 is the last. As a consequence, the 1D inversion results in a deep conductive body laterally shifted relative to its true position (artifact 1 in Figure 9b). Zone 4 presents a similar context as zone 1 for a transition between a thin peat deposit and a thicker peat deposit. Zones 2, 3, and 5 (especially zone 3) show complex 2D/3D responses due to lateral variations of the conductivity that are smaller than the footprint of each configuration. For example,

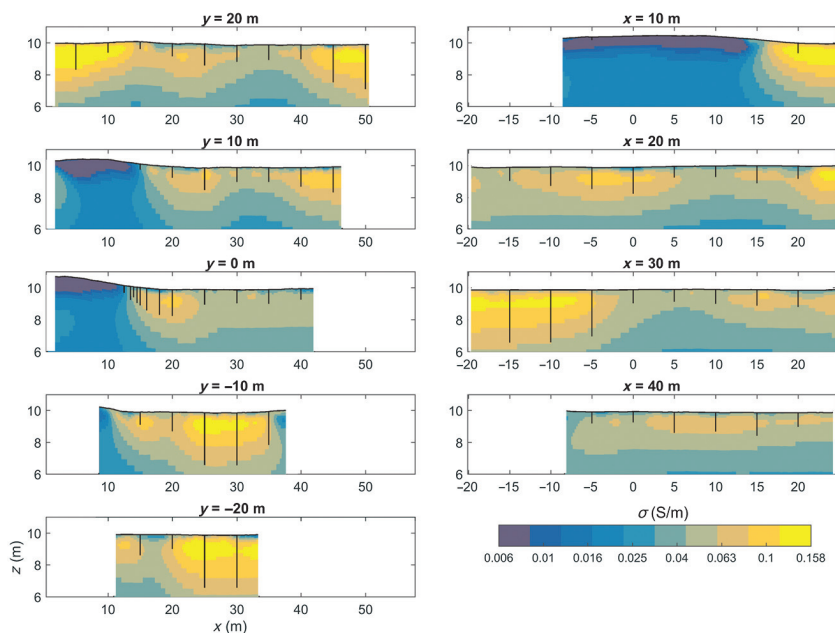


Figure 8. Results of 3D MCD imaging of our field data set visualized using selected inline and crossline slices through the final 3D model. The vertical slices are compared with the peat thickness as observed in boreholes (black vertical bars). The locations of the profiles are illustrated in Figure 7a.

in such a context, the HCP responses show an anomaly composed of a central downward peak surrounded by two upward peaks. The PERP responses show a single noncentered upward peak. Once the four configurations of the present system are taken together, we can see (clearly in zone 3) that the two PERP noncentered upward peaks coincide with the first noncentered upward peaks of the two HCP anomalies. To fit this max-min-max feature of the HCP channels, the 1D inversion has to define more conductivity at the flanks and less conductivity in the middle. Furthermore, to fit the left-skewed PERP signal, the 1D inversion has to increase the conductivity more on the left side than on the right side. In contrast, the 3D linear inversion fits all these signal forms with a single local maximum in conductivity at $x = 25$ m.

Overall, the 1D outcome can lead to an interpretation of the thickness of the peat deposit, which is not in accordance with the trend observed by our borehole and GPR data. The presence of these artifacts as well as the good 1D data fit clearly illustrate how the 1D nonlinear inversion can be more limited than the present 3D linear approach even in a weak 2D/“quasi-1D” context as often encountered in soil sciences or hydrology. To summarize, in the present context, the nonlinear 1D and the MCD provide approximate solutions, but the MCD correctly images the structural characteristics present at our field site (Figure 9c). By merging the results obtained by the 3D inversion of EMI data, the GPR profile analysis and the drillhole peat-thickness data, we could build the geologic model as shown in Figure 9d.

DISCUSSION

Limitations of the 3D linear MCD method

Our method assumes the validity of the LIN approximation; i.e., sensor spacing, source frequency, and ground conductivity together must fulfill equation 1. Moreover, it underestimates the conductivity of isolated bodies that are more conductive than the background. Data must be sampled densely and with high relative position accuracy to honor the sophisticated 2D lateral deconvolution of signal waveforms. Because the computation is based on deconvolution via the 2D Fourier transform, the data domain must be large, and the method does not work well close to the edges of the measured grid. Even for a large grid in a generally moderate-conductivity regime such as the field example above, some preprocessing is mandatory, in which responses from metallic object (not fulfilling equation 2) are recognized and removed. In addition, the grids are padded by smooth extrapolation to rectangular grids as needed for a 2D Fourier transform.

Merits of the 3D linear MCD method

As long as equations 1 and 2 are fulfilled, it allows the robust characterization of structural properties of the subsurface conductivity distribution. The inverse computations are almost instantaneous. The kernels $\psi(x, y, z)$ can be precomputed for a specific field instrument. The remaining forward and inverse Fourier transforms and matrix

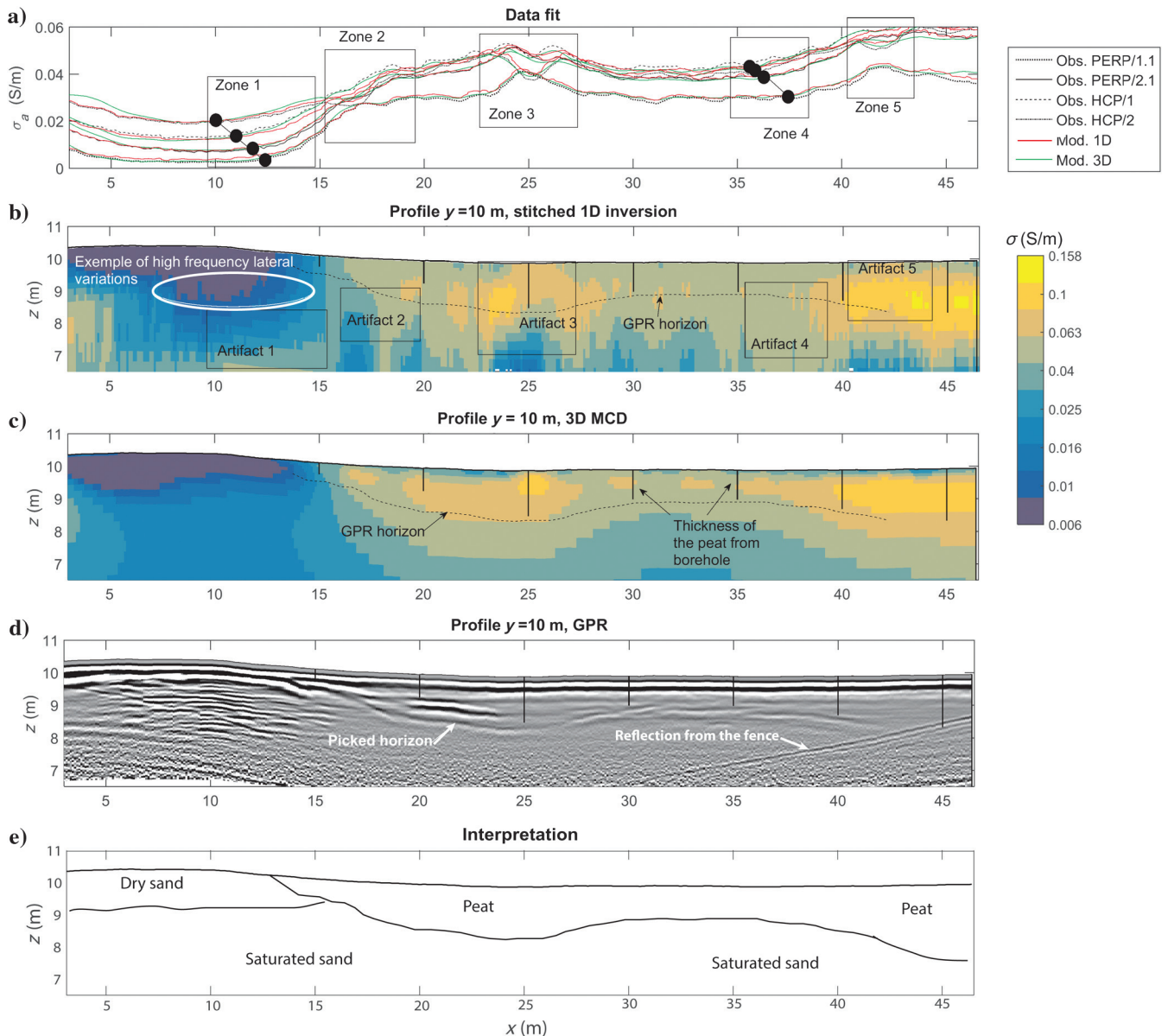


Figure 9. Comparison between the 3D MCD imaging, the 1D nonlinear inversion result, a GPR profile, and the peat thickness observed in several boreholes for a selected profile at $y = 10$ m: (a) observed and modeled data along the profile. The 1D and 3D inversions were set to fit the data with a relative rms within 4%–5%. The rectangles delimit areas where the 2D/3D effects are identified. The black dots correspond to the position at which the system detects the lateral contrast located further in the profile, (b) result of the point-by-point 1D nonlinear inversion for 25 layers with vertical smoothness constraints. The rectangles delimit the 2D/3D artifacts related to the lateral variation of conductivity, (c) result of our 3D MCD method, (d) GPR section on the same profile, and (e) geologic interpretation.

multiplications will run at a speed similar to the rendering of the associated displays of the resulting 3D model cube. It follows that this method is a natural near-instant inversion of LIN-EMI data. Subsequently, users may choose also to do nonlinear modeling such as the much slower point-by-point 1D inversion, keeping in mind that it will fail where the fast 3D MCD predicts rapid lateral variations.

Extending the application domain to higher conductivity

If the subsurface is characterized by high conductivities resulting in induction numbers exceeding the LIN condition, it is possible to

compute sensitivity kernels using a Born approximation not relative to conductivity fulfilling the LIN condition but relative to this higher average conductivity. This will extend the validity of the MCD provided that the 3D conductivity anomalies are not too strong (according to equation 2).

CONCLUSION

A fast 3D MCD method was applied to electromagnetic loop-loop data. Synthetic tests performed at LINS, as it is found in many applications including soil sciences, hydrology, and archaeology, showed that the inversion method gave a very satisfactory resolution

of structure at wavelengths of the order of the tool length. This contrasted the commonly used point-by-point 1D nonlinear inversion that suffers from notorious 2D/3D artifacts, and it even gave opposite polarities when applied to a laterally oscillating test pattern. A field test confirmed these findings. A four-configuration data set sampled with spacing of 0.1×0.5 m was interpolated to 0.1×0.1 m and extrapolated to 1000×1000 samples before deconvolution. The fast 3D MCD delivered simple structure in good agreement with 62 drillings and produced a data fit within 4%–5%. For comparison, the 389,880 sounding points were inverted by a 1D nonlinear inversion method. The resulting model volume showed several examples of artifacts characterized by small-scale variations in conductivity.

Where the LIN condition is fulfilled and contrasts are moderate, our 3D inversion approach will yield significant lateral focusing of conductivity structure and vertical resolution, depending on the number of configurations available. Where contrasts and induction numbers are higher, this inversion will not be quantitatively correct, but the lateral focusing will still reveal the most important structural characteristics. We therefore propose that regularly sampled loop-loop EMI data are routinely subjected to this very rapid inverse modeling method. Often this inversion will be of sufficient quality; under all circumstances, it will provide a first estimate before sophisticated nonlinear inversion procedures — preferably multidimensional — are applied.

ACKNOWLEDGMENTS

The authors are grateful to P. Koyan for collecting the EMI data set in Paulinenau during his bachelor thesis and to M. Dubnitzki for performing the drillholes.

REFERENCES

- Aster, R. C., B. Borchers, and C. H. Thurber, 2005, Parameter estimation and inverse problems: Elsevier Academic Press.
- Auken, E., A. V. Christiansen, B. H. Jacobsen, N. Foged, and K. I. Sorensen, 2005, Piecewise 1D laterally constrained inversion of resistivity data: *Geophysical Prospecting*, **53**, 497–506, doi: [10.1111/j.1365-2478.2005.00486.x](https://doi.org/10.1111/j.1365-2478.2005.00486.x).
- Böniger, U., and J. Tronicke, 2010, On the potential of kinematic GPR surveying using a self-tracking total station: Evaluating system crosstalk and latency: *IEEE Transactions on Geoscience and Remote Sensing*, **48**, 3792–3798, doi: [10.1109/TGRS.2010.2048332](https://doi.org/10.1109/TGRS.2010.2048332).
- Constable, S. C., R. L. Parker, and C. G. Constable, 1987, Occams inversion: A practical algorithm for generating smooth models from electromagnetic sounding data: *Geophysics*, **52**, 289–300, doi: [10.1190/1.1442303](https://doi.org/10.1190/1.1442303).
- Dabas, M., A. Anest, J. Thiesson, and A. Tabbagh, 2016, Slingram EMI devices for characterizing resistive features using apparent conductivity measurements: Check of the dualem-421s instrument and field tests: *Archaeological Prospection*, **23**, 165–180, doi: [10.1002/arp.v23.3](https://doi.org/10.1002/arp.v23.3).
- Dafflon, B., S. Hubbard, C. Ulrich, J. Peterson, Y. Wu, H. Wainwright, and T. J. Kneafsey, 2016, Geophysical estimation of shallow permafrost distribution and properties in an ice-wedge polygon-dominated arctic tundra region: *Geophysics*, **81**, no. 1, WA247–WA263, doi: [10.1190/geo2015-0175.1](https://doi.org/10.1190/geo2015-0175.1).
- Davies, G., J. Huang, F. A. M. Santos, and J. Triantafyllis, 2015, Modeling coastal salinity in quasi 2D and 3D using a DUALEM-421 and inversion software: *Groundwater*, **53**, 424–431, doi: [10.1111/gwat.12231](https://doi.org/10.1111/gwat.12231).
- De Smedt, P., M. Van Meirvenne, T. Saey, E. Baldwin, C. Gaffney, and V. Gaffney, 2014, Unveiling the prehistoric landscape at Stonehenge through multi-receiver EMI: *Journal of Archaeological Science*, **50**, 16–23, doi: [10.1016/j.jas.2014.06.020](https://doi.org/10.1016/j.jas.2014.06.020).
- Delefortrie, S., P. De Smedt, T. Saey, E. Van de Vijver, and M. Van Meirvenne, 2014, An efficient calibration procedure for correction of drift in EMI survey data: *Journal of Applied Geophysics*, **110**, 115–125, doi: [10.1016/j.jappgeo.2014.09.004](https://doi.org/10.1016/j.jappgeo.2014.09.004).
- Delefortrie, S., T. Saey, J. De Pue, E. Van de Vijver, P. De Smedt, and M. Van Meirvenne, 2016, Evaluating corrections for a horizontal offset between sensor and position data for surveys on land: *Precision Agriculture*, **17**, 349–364, doi: [10.1007/s11119-015-9423-8](https://doi.org/10.1007/s11119-015-9423-8).
- El-Qady, G., M. Metwaly, and A. Khozaym, 2014, Tracing buried pipelines using multi frequency electromagnetic: *NRIAG Journal of Astronomy and Geophysics*, **3**, 101–107, doi: [10.1016/j.nrjag.2014.06.002](https://doi.org/10.1016/j.nrjag.2014.06.002).
- Grellier, S., N. Florsch, C. Camerlynck, J. L. Janeau, P. Podwojewski, and S. Lorentz, 2013, The use of Slingram EM38 data for topsoil and subsoil geoelectrical characterization with a Bayesian inversion: *Geoderma*, **200–201**, 140–155, doi: [10.1016/j.geoderma.2013.01.020](https://doi.org/10.1016/j.geoderma.2013.01.020).
- Guillemoteau, J., P. Sailhac, and M. Behaegel, 2015a, Modelling an arbitrarily oriented magnetic dipole over an homogenous half-space for a rapid topographic correction of airborne EM data: *Exploration Geophysics*, **46**, 85–96, doi: [10.1071/EG13093](https://doi.org/10.1071/EG13093).
- Guillemoteau, J., P. Sailhac, C. Boulanger, and J. Trules, 2015b, Inversion of ground constant offset loop-loop electromagnetic data for a large range of induction numbers: *Geophysics*, **80**, no. 1, E11–E21, doi: [10.1190/geo2014-0005.1](https://doi.org/10.1190/geo2014-0005.1).
- Guillemoteau, J., F. X. Simon, E. Lück, and J. Tronicke, 2016, 1D sequential inversion of portable multi-configuration electromagnetic induction data: *Near Surface Geophysics*, **14**, 411–420, doi: [10.3997/1873-0604.2016029](https://doi.org/10.3997/1873-0604.2016029).
- Guillemoteau, J., and J. Tronicke, 2015, Non-standard ground conductivity meter configurations: Evaluating sensitivities and applicability: *Journal of Applied Geophysics*, **118**, 15–23, doi: [10.1016/j.jappgeo.2015.04.008](https://doi.org/10.1016/j.jappgeo.2015.04.008).
- Guillemoteau, J., and J. Tronicke, 2016, Evaluation of a rapid hybrid spectral-spatial domain 3D forward modeling approach for loop-loop electromagnetic induction quadrature data acquired in low-induction-number environments: *Geophysics*, **81**, no. 6, E447–E458, doi: [10.1190/geo2015-0584.1](https://doi.org/10.1190/geo2015-0584.1).
- Habashy, T. M., R. W. Groom, and B. R. Spies, 1993, Beyond the Born and Rytov approximation: A nonlinear approach to electromagnetic scattering: *Journal of Geophysical Research*, **98**, 1759–1775, doi: [10.1029/92JB02324](https://doi.org/10.1029/92JB02324).
- Hunkeler, P. A., S. Hendricks, M. Hoppmann, C. G. Farquharson, T. Kalscheuer, M. Grab, M. S. Kaufmann, L. Rabenstein, and R. Gerdes, 2016, Improved 1D inversions for sea ice thickness and conductivity from electromagnetic induction data: Inclusion of nonlinearities caused by passive bucking: *Geophysics*, **81**, no. 1, WA45–WA58, doi: [10.1190/geo2015-0130.1](https://doi.org/10.1190/geo2015-0130.1).
- Jadoon, K. Z., D. Moghadas, A. Jadoon, T. M. Missimer, S. K. Al-Mashharawi, and M. F. McCabe, 2015, Estimation of soil salinity in a drip irrigation system by using joint inversion of multicoil electromagnetic induction measurements: *Water Resources Research*, **51**, 3490–3504, doi: [10.1002/2014WR016245](https://doi.org/10.1002/2014WR016245).
- Kamm, J., M. Becken, and L. B. Pedersen, 2013, Inversion of slingram electromagnetic induction data using a Born approximation: *Geophysics*, **78**, no. 4, E201–E212, doi: [10.1190/geo2012-0484.1](https://doi.org/10.1190/geo2012-0484.1).
- McGillivray, P. R., D. W. Oldenburg, R. G. Ellis, and T. M. Habashy, 1994, Calculation of sensitivities for the frequency-domain electromagnetic problem: *Geophysical Journal International*, **116**, 1–4, doi: [10.1111/j.1365-246X.1994.tb02121.x](https://doi.org/10.1111/j.1365-246X.1994.tb02121.x).
- McKenna, S. P., and J. R. McKenna, 2010, Modeling and analysis of the response of a triaxial, frequency-domain electromagnetic induction sensor to a buried linear conductor: *Geophysics*, **75**, no. 1, F1–F14, doi: [10.1190/1.3267876](https://doi.org/10.1190/1.3267876).
- Menke, W., 1989, *Geophysical data analysis: Discrete inverse theory*: Academic Press.
- Møller, I., B. H. Jacobsen, and N. B. Christensen, 2001, Rapid inversion of 2-D geoelectrical data by multichannel deconvolution: *Geophysics*, **66**, 800–808, doi: [10.1190/1.1444969](https://doi.org/10.1190/1.1444969).
- Pedreira-Parrilla, A., E. Van De Vijver, M. Van Meirvenne, A. J. Espejo-Pérez, J. V. Giráldez, and K. Vanderlinden, 2016, Apparent electrical conductivity measurements in an olive orchard under wet and dry soil conditions: Significance for clay and soil water content mapping: *Precision Agriculture*, **17**, 531–545, doi: [10.1007/s11119-016-9435-z](https://doi.org/10.1007/s11119-016-9435-z).
- Pérez-Flores, M. A., R. G. Antonio-Carpio, E. Gómez-Trevino, I. Ferguson, and S. Méndez-Delgado, 2012, Imaging of 3D electromagnetic data at low-induction numbers: *Geophysics*, **77**, no. 4, WB47–WB57, doi: [10.1190/geo2011-0368.1](https://doi.org/10.1190/geo2011-0368.1).
- Pérez-Flores, M. A., S. Méndez-Delgado, and E. Gómez-Trevino, 2001, Imaging low frequency and DC electromagnetic fields using a simple linear approximation: *Geophysics*, **66**, 1067–1081, doi: [10.1190/1.1487054](https://doi.org/10.1190/1.1487054).
- Raiche, A., 2008, The P223 software suite for planning and interpreting EM surveys: *Previews*, **132**, 25–30.
- Rezaei, M., T. Saey, P. Seuntjens, I. Joris, W. Boëne, M. Van Meirvenne, and W. Cornelis, 2016, Predicting saturated hydraulic conductivity in a sandy grassland using proximally sensed apparent electrical conductivity: *Journal of Applied Geophysics*, **126**, 35–41, doi: [10.1016/j.jappgeo.2016.01.010](https://doi.org/10.1016/j.jappgeo.2016.01.010).
- Rudin, W., 1987, *Real and complex analysis*: McGraw Hill.
- Rudolph, S., C. Wongleecharoen, R. Lark, B. Marchant, S. Garr, M. Herbst, H. Vereecken, and L. Weierhiller, 2016, Soil apparent conductivity measurements for planning and analysis of agricultural experiments: A case

- study from western-thailand: *Geoderma*, **267**, 220–229, doi: [10.1016/j.geoderma.2015.12.013](https://doi.org/10.1016/j.geoderma.2015.12.013).
- Saey, T., P. De Smedt, M. Monirul Islam, E. Meerschman, E. Van de Vijver, A. Lehouck, and M. Van Meirvenne, 2012, Depth slicing of multi-receiver EMI measurements to enhance the delineation of contrasting subsoil features: *Geoderma*, **189**, 514–521, doi: [10.1016/j.geoderma.2012.06.010](https://doi.org/10.1016/j.geoderma.2012.06.010).
- Santos, F. A. M., 2004, 1-D laterally constrained inversion of EM34 profiling data: *Journal of Applied Geophysics*, **56**, 123–134.
- Scollar, I., A. Tabbagh, A. Hesse, and I. Herzog, 1990, *Archaeological prospecting and remote sensing*: Cambridge University Press.
- Shubitidze, F., K. O'Neill, I. Shamatava, K. Sun, and K. D. Paulsen, 2005, Fast and accurate calculation of physically complete EMI response by a heterogeneous metallic object: *IEEE Transactions on Geoscience and Remote Sensing*, **43**, 1736–1750, doi: [10.1109/TGRS.2005.851176](https://doi.org/10.1109/TGRS.2005.851176).
- Simon, F. X., A. Sarris, J. Thiesson, and A. Tabbagh, 2015, Mapping of quadrature magnetic susceptibility/magnetic viscosity of soils by using multi-frequency EMI: *Journal of Applied Geophysics*, **120**, 36–47, doi: [10.1016/j.jappgeo.2015.06.007](https://doi.org/10.1016/j.jappgeo.2015.06.007).
- Tarantola, A., and B. Valette, 1982, Generalized nonlinear inverse problems solved using the least squares criterion: *Reviews of Geophysics*, **20**, 219–232, doi: [10.1029/RG020i002p00219](https://doi.org/10.1029/RG020i002p00219).
- Thiesson, J., P. Kessouri, C. Schamper, and A. Tabbagh, 2014, Calibration of frequency domain electromagnetic devices used in near-surface surveying: *Near Surface Geophysics*, **12**, 481–491, doi: [10.3997/1873-0604.2014012](https://doi.org/10.3997/1873-0604.2014012).
- Tølbøll, R. J., and N. B. Christensen, 2007, Sensitivity functions of frequency-domain magnetic dipole-dipole systems: *Geophysics*, **72**, no. 2, F45–F56, doi: [10.1190/1.2409623](https://doi.org/10.1190/1.2409623).
- Vereecken, H., J. A. Huisman, H. J. Hendricks Franssen, N. Brüggemann, H. R. Bogaen, S. Kollet, M. Javaux, J. van der Kruk, and J. Vanderborght, 2015, Soil hydrology: Recent methodological advances, challenges, and perspectives: *Water resources research*, **51**, 2616–2633, doi: [10.1002/2014WR016852](https://doi.org/10.1002/2014WR016852).
- von Hebel, C., S. Rudolph, A. Mester, J. Huisman, P. Kumbhar, H. Vereecken, and J. van der Kruk, 2014, Three-dimensional imaging of subsurface structural patterns using quantitative large-scale multiconfiguration electromagnetic induction data: *Water Resources Research*, **50**, 2732–2748, doi: [10.1002/2013WR014864](https://doi.org/10.1002/2013WR014864).
- Ward, S. H., and G. W. Hohmann, 1988, Electromagnetic theory for geophysical applications, in M. N. Nabighian, ed., *Electromagnetic methods in applied geophysics theory*: SEG, 131–311.
- West, G. F., and J. C. Macnae, 1991, Physics of the electromagnetic induction exploration method, in M. N. Nabighian, ed., *Electromagnetic methods in applied geophysics applications, parts A and part B*: SEG, 5–45.
- Weymer, B. A., M. E. Everett, T. S. de Smet, and C. Houser, 2015, Review of electromagnetic induction for mapping barrier island framework geology: *Sedimentary Geology*, **321**, 11–24, doi: [10.1016/j.sedgeo.2015.03.005](https://doi.org/10.1016/j.sedgeo.2015.03.005).